Intelligent and Automatic In Vivo Detection and Quantification of Transplanted Cells in MRI

Muhammad Jamal Afridi,[1] Arun Ross,[1] Xiaoming Liu,[1] Margaret F. Bennewitz,[2] Dorela D. Shuboni,[3] and Erik M. Shapiro[3]*

Purpose: Magnetic resonance imaging (MRI)-based cell tracking has emerged as a useful tool for identifying the location of transplanted cells, and even their migration. Magnetically labeled cells appear as dark contrast in T2*-weighted MRI, with sensitivities of individual cells. One key hurdle to the widespread use of MRI-based cell tracking is the inability to determine the number of transplanted cells based on this contrast feature. In the case of single cell detection, manual enumeration of spots in three-dimensional (3D) MRI in principle is possible; however, it is a tedious and time-consuming task that is prone to subjectivity and inaccuracy on a large scale. This research presents the first comprehensive study on how a computer-based *intelligent*, *automatic,* and *accurate* cell quantification approach can be designed for spot detection in MRI scans.
Methods: Magnetically labeled mesenchymal stem cells (MSCs) were transplanted into rats using an intracardiac injection, accomplishing single cell seeding in the brain. T2*-weighted MRI of these rat brains were performed where labeled MSCs appeared as spots. Using machine learning and computer vision paradigms, approaches were designed to systematically explore the possibility of automatic detection of these spots in MRI. Experiments were validated against known in vitro scenarios.
Results: Using the proposed deep convolutional neural network (CNN) architecture, an in vivo accuracy up to 97.3% and in vitro accuracy of up to 99.8% was achieved for automated spot detection in MRI data.
Conclusion: The proposed approach for automatic quantification of MRI-based cell tracking will facilitate the use of MRI in large-scale cell therapy studies. **Magn Reson Med 00:000–000, 2016. © 2016 International Society for Magnetic Resonance in Medicine.**

Key words: Machine learning; cell therapy; MRI; iron oxide

INTRODUCTION

Cell-based therapies are poised to make a significant impact across a broad spectrum of medical scenarios. In regenerative medicine, stem cell transplants are in various stages of clinical trials for treating or slowing a myriad of diseases, including Parkinson's disease (1,2), rheumatoid arthritis (3,4), and multiple sclerosis (5,6). Cell-based therapy in the form of cancer immunotherapy is also being tested in clinical trials (7,8). It is well acknowledged that imaging the *location* of transplanted cells, both immediately and serially after delivery, will be a crucial component for monitoring the success of the treatment. Two important applications for imaging transplanted cells are:

1. to noninvasively *quantify the number of cells* that were delivered or that homed to a particular location, and
2. to serially determine if there are cells that are leaving desirable or intended locations and entering undesirable locations.

For multiple reasons, including image resolution, lack of radiation, and established safety and imaging versatility, magnetic resonance imaging (MRI) has emerged as the most popular and perhaps most promising modality for tracking cells in vivo following transplant or delivery. In general, MRI-based detection of cells is accomplished by first labeling cells with superparamagnetic iron oxide nanoparticles or microparticles, though some cell types can be labeled directly in vivo, such as neural progenitor cells. Following transplant, these labeled cells are then detected in an MRI using imaging sequences where the signal intensity is sensitive to the local magnetic field inhomogeneity caused by the iron oxide particles. This results in dark contrast in the MRI (9,10). In the case of a transplant of large numbers of magnetically labeled cells, large areas of dark contrast are formed. In the case of isolated cells, given sufficient magnetic labeling and high image resolution, in vivo single cell detection is possible, indicated by a well-defined and well characterized dark spot in the image (See Fig. 1).

Due to the rather complex relationship between iron content, particle distribution, iron crystal integrity, distribution of magnetic label and cells, and soforth, it is difficult to quantify cell numbers in an MRI-based cell tracking experiment. This is especially the case for a single graft with a large number of cells. There are efficient methods of quantifying iron content, most notably using SWIFT based imaging (11), but the direct correlation to cell number is not straightforward, due to the reasons listed above. MRI-based detection of single cells presents a much more direct way of enumerating cells in certain cell therapy type applications, such as hepatocyte transplant (10), or for immune cells that have homed to an organ or a tumor (12). In this case, the solution is
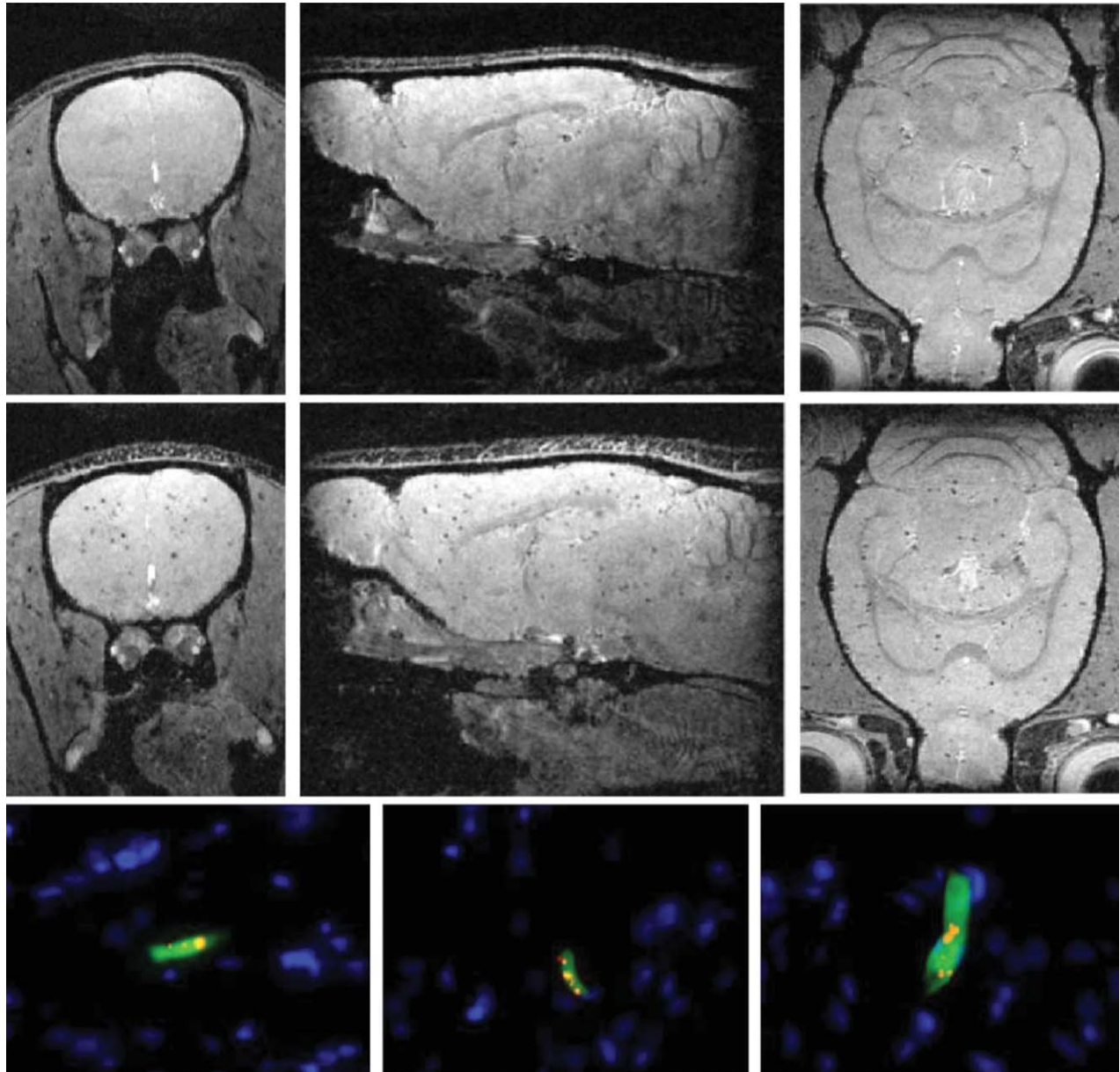
FIG. 1. Three orthogonal MRI slices extracted from 3D data sets of the brain from animals injected with unlabeled MSCs (top row) and magnetically labeled MSCs (middle row). Note the labeled MSCs appear as distributed dark spots in the brain unlike unlabeled MSCs. The bottom row shows three different fluorescence histology sections from animals injected with magnetically labeled MSCs confirming that these cells were present in the brain mostly as isolated, single cells. Blue indicates cell nuclei, green is the fluorescent label in the cell, red is the fluorescent label of the magnetic particle (See the Supporting Information Fig. S1 for details).

straightforward: if dark spots in the MRI are from single cells, then counting these spots in the MRI should yield cell number. While seemingly straightforward, performing such quantitative analysis on three-dimensional (3D) data sets is a difficult task that cannot be accomplished using traditional manual methodologies. Manual analysis and enumeration of cells in MRI is tedious, laborious, and also limited in capturing patterns of cell behavior. In this respect, a manual approach cannot be adopted to analyze *large scale* datasets comprising dozens of research subjects. Various commercial software that are currently available for MRI can only assist a medical expert in conducting manual analysis. The problem is

further compounded in the case of eventual MRI detection of single cells at clinical resolution, which is lower than that achieved on high field small animal systems. At lower image resolution, the well-defined, well-characterized dark spot loses shape and intensity and can be difficult to manually define in a large number of MRI slices.

These hurdles highlight the pressing need to develop an *automatic* and *intelligent* approach for detecting and enumerating transplanted cells in MRI, meeting all the aforementioned challenges. An automatic and intelligent approach can allow researchers to efficiently conduct large scale analysis of transplanted cells in MRI,

Table 1
Collection Details and Characteristics of our MRI Database

Set	Type	Subject	Labeler	Machine	Labeled scans	Total labels	Resolution	Size
G_A	in vivo	Brain	R_1	11.7T	$G_{1A}, G_{2A}, G_{3A}, G_{4A}, G_{5A}$	15,442	100 μm	$256 \times 256 \times 256$
G_B	in vivo	Brain	R_2	7T	G_{1B}, G_{2B}	2992	100 μm	$256 \times 200 \times 256$
G_C	in vitro	Tube	R_2	7T	$G_{1C}, G_{2C}, G_{3C}, G_{4C}$	814	100 μm	$128 \times 80 \times 80$
G_D	in vitro	Tube	R_2	7T	$G_{1D}, G_{2D}, G_{3D}, G_{4D}$	514	200 μm	$64 \times 40 \times 40$
G_E	in vitro	Tube	$\bar{t}$	7T	$G_{1E}, G_{2E}, G_{3E} \ldots, G_{25E}$	(2400×25)	100 μm	$100 \times 64 \times 64$

facilitating the exploration of new transplant paradigms and cell sources. Such generalized intelligent tools will find use across a broad spectrum of biomedical pursuits. However, the unique challenges of designing such a tool has not been addressed in any prior literature, especially in the context of detecting cells in MRI.

To design and evaluate an intelligent and automatic approach for cell spot detection in MRI, ground truth definitions, i.e., labels, that annotate spots in MRI images, are required. In (13), authors recognized the need for automation and adopted a threshold-based strategy for automatically detecting spots in MRI. However, their approach was not evaluated using a ground truth. Although such threshold reliant approaches are not known to be intelligent for handling variations and diversity in data, their study in fact highlights the need for automation (14,15). Automatic machine learning (ML) approaches have been successfully used in a wide range of image analysis applications (14,16,17). However, it is unexplored how such approaches can be appropriated to the problem of MRI spot detection. Further, state-of-the-art ML approaches rely on a large volume of training data for accurate learning. Unfortunately, due to practical limitations, generating large-scale annotated data is challenging in both preclinical and the clinical arenas. Annotation can also be prohibitively time consuming and can only be performed by a medical expert. Hence, crowd sourcing approaches such as the use of Amazon's Mechanical Turk (18), cannot be adopted for annotation in such applications. Therefore, the problem of spot detection using a *limited* amount of annotated training data, is an additional unaddressed challenge. In summary, the problem of 3D spot detection in MRI presents the following key challenges:

1. **Candidate region extraction**: Given an MRI scan, how can all the candidate regions that can potentially contain a spot be effectively and efficiently extracted?
2. **Feature design**: What will be the best feature representation to accurately capture the interclass appearance variations of spots in MRI?
3. **Dataset collection**: Intelligent ML approaches will require annotated (labeled) MRI datasets for spot detection. Therefore, a diverse set of MRI scans need to be collected and labels must be obtained on them.
4. **Learning with limited data**: Further, how can state-of-the-art ML approaches learn to detect spots in MRI despite using very *limited* MRI data for training?

This article addresses these challenges of automated spot detection in MRI and presents the first comprehensive study to investigate *how* different ML approaches encompassing three different paradigms, can be utilized for this purpose. Experimental results of the approaches proposed in this article show that spots can be automatically detected using ML techniques in unseen in vivo MRI scans with an accuracy of up to 97.3%.

METHODS

Datasets

As shown in Table 1, a diverse set of 33 in vitro MRI scans of gel samples and 7 in vivo MRI scans of rat brains with transplanted stem cells were utilized in this study. More than 19,700 manual ground truth labels were collected on 15 of these scans ($G_A - G_D$). A flexible software tool (with image pan, zoom, slice advance, contrast manipulation, etc.) was specifically designed to allow our medical expert to put a mouse cursor over a spot in an MRI and click the mouse button to record that spot. These clicked points are taken as our ground truth (labels) on spots in MRI. In addition, theoretically computed cell numbers on 25 scans were also utilized as ground truths during the approach evaluation.

In vitro: Imaging phantoms were constructed consisting of a known number of 4.5-micron diameter, magnetic microparticles with 10 pg iron per particle, suspended in agarose samples. Each microparticle approximates a single magnetically labeled cell with appropriate iron content for MRI-based single cell detection (19). T2*-weighted gradient echo MRI was then performed on these samples at a field strength of 7T.

As can be seen in Table 1, these scans have variation in resolution, matrix sizes, and amount of spots (labels). G_E has 25 data sets, collected from five samples under five different MRI conditions. These conditions were variations in TE from 10–30 ms (signal to noise >30:1), and images with low signal to noise ratio (~8:1) at TE = 10 and 20. The effect of increasing TE is to enhance the size of the spots. The higher the TE, the larger the spot (19). The downside of higher TE is that the physics which governs enlargement of the spot, the difference in magnetic susceptibility between the location in and around the magnetic particles and the surrounding tissue, also causes the background tissue to darken. The rationale to collect images with both high and low signal to noise ratio is to test the robustness of our spot detection procedure in two potential in vivo scenarios. Manual ground truths were collected from experts on eight in vitro MRI scans of G_C and G_D. These sets were used for training and evaluating ML approaches. For G_E, the theoretically computed ground truth was known. This set was used

for a direct comparison between the automatically detected spots and the theoretically expected.

In vivo: Two different sets of in vivo MRI were collected from two different machines having different field strengths. Using one machine with a field strength of 11.7T, five MRI scans of rats were collected, which are represented by G_A in Table 1. Three of them were injected intracardiac $1 - 1.5$ h prior to the scan with rat mesenchymal stem cells (MSCs) that had been labeled with micron sized iron oxide particles (MPIOs) to a level of ∼14 pg iron per cell. This transplantation scheme delivers cells to the brain—an intravenous injection would deliver cells only to the liver and lungs. Two additional rats were not injected at all. Using another machine with 7T, two further brain MRI scans of rats were collected, similarly previously transplanted with MPIO labeled MSCs. G_B represents these two scans in Table 1. The rationale behind collecting these two different in vivo sets was to be able to validate the generalization and robustness of our learned algorithm against potential variations arising from different imaging systems. Note that a different amount of MSCs were injected in different rats to achieve further variations in the data. All MRI were 3D T2*-weighted gradient echo. Further details regarding cell labeling, cell transplant, in vivo MRI and histology are in Supporting Information.

Machine Learning Methods

In machine learning, a classification approach maps a real-world problem into a classification task where two or more entities (classes) are to be intelligently distinguished from each other (see (20) for basic details). For example, classifying potential candidate regions in MRI as spots or nonspots will also be a classification task.

In the context of this work, classification paradigms can be categorized into three fundamental paradigms. In the first paradigm (P-1), discriminating information is extracted from the images using a predefined approach that is designed by an expert based on intuition and experience. This information may be in the form of a numeric array of values known as *features*. For each image, such features along with their ground truth classification labels are then forwarded to another algorithm called *classifier* or *classification technique* which learns to distinguish between the classes. A classifier can be learned mathematical functions, set of if-then rules, and soforth.

In the second paradigm (P-2), the feature representations are not manually designed by an expert but rather automatically learned from the data. Generally, both, feature representations and the classifiers are learned automatically in a single unified framework. Many neural network-based approaches fall into this category which can take image datasets directly as input, along with the labels, and learn a classification model.

In a third classification paradigm (P-3), the model can be learned in the same manner as in P-1 or P-2. The difference here is that learning the model requires more than just the given task's data (MRI data in this case). Available labeled data for other tasks such as face recognition, that may not be directly related to the given task,

is exploited using a *transfer learning* approach. This approach is useful when collecting large scale annotated data is challenging.

The general architecture of this study and the differences between the ML paradigms are summarized in Figure 2. Candidate regions $X = \{\cup x_i\}_{i=1}^n$ are located and extracted from an MRI scan G using the approach proposed in this study. Each candidate region x_i may or may not contain a spot. Therefore, all candidate regions in X, along with their manual ground truth labels $Y = \{\cup y_i\}_{i=1}^n, y_i \in \{1, 0\}$, are then forwarded to each of the three machine learning paradigms for learning a model M. Depending on the paradigm, this model may be based on a set of if-then rules, mapping functions, a sequence of convolutional filters, and soforth. For example, in the context of convolutional neural network (CNN), the model M can take a candidate region as an input and apply a sequence of learned convolutional filters and transformation functions to finally output a value that either describes the candidate region as a spot or a nonspot. Thus, once M is learned, the proposed approach can automatically locate, extract and detect spots in any unseen MRI.

Candidate Generation Using Superpixels

The first challenge in this research is to define a candidate region. Processing each pixel as a candidate region can result in a huge computational burden. We addressed this issue by extracting superpixels (32) as classification units from each MRI scan (15). A superpixel technique groups locally close pixels with similar intensities into a single unit. As spots are usually darker than their surrounding, they are characterized as superpixels with lower average intensity than the surrounding superpixels. Based on this idea, a novel set of features based on the superpixel intensities, was designed. Experimental results show that these features provide superior performance for spot detection compared to the approach in (14). However, this approach has the following limitations: (A) The accuracy of the approach was dependent on the preciseness of the superpixel algorithms. (B) The approach assumes a superpixel based model for a spot in terms of its depth across consecutive MRI slices. This does not hold true for all spots in different MRI settings.

The strategy adopted in this article is resilient to imprecisions in the superpixel extraction algorithms. Based on each superpixel unit, a representative patch is extracted from the MRI scan as explained in Figure 3. Each patch is then taken as a candidate region and undergoes a feature extraction process. The approach is *model-free* and imitates the strategy adopted by a human labeler. All candidate patches are first detected in 2D MRI slices and then neighboring patches detected in consecutive slices are connected without imposing any restriction on their depth in 3D.

The spatial location of each patch in MRI is also recorded. Consequently, these extracted patches are forwarded to the machine learning algorithms as input data.

In summary, the first two paradigms focus on how to accurately and automatically distinguish spot patches from nonspot patches. Then using the 3rd ML paradigm, i.e., transfer learning, we investigated how the best approach out of the first two paradigms could be adapted
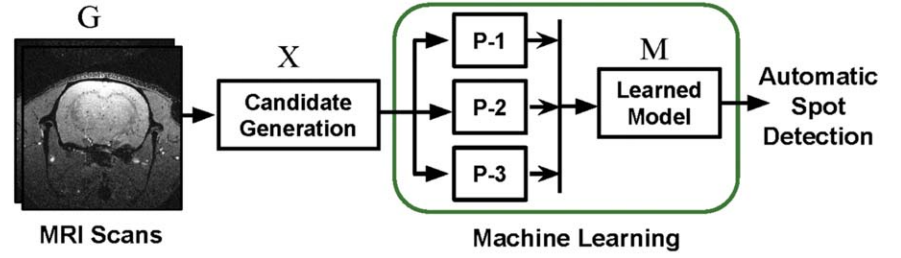
FIG. 2. (Top) Basic architecture: Three different ML paradigms P-1, P-2, and P-3 are explored to learn a spot detection model. (Bottom) Fundamental design phase differences between the three ML paradigms.

	P-1	P-2	P-3
Training Data	MRI Data Only	MRI data Only	MRI Data + Other Unrelated Data
Features and Classifier	Fixed	Learned	Fixed or Learned

to achieve better results despite using very limited training data.

RESULTS

Spot Detection with Fixed Designs (P-1)

This is the traditional and most widely adopted paradigm in computer vision and pattern recognition based studies (14,15). In this article, an elaborate set of feature extraction methods are utilized that extract shape, intensity, texture, and context information about the entities in the candidate patches. In the attached Supporting Information Figures S2–S4 present a brief explanation on how hand-designed features can be extracted specifically for the task of capturing *spot appearance* in MRI.

Extracted features are finally concatenated to form a feature vector for each candidate patch x_i. From this feature vector, the most useful features are selected and the irrelevant features are eliminated using a feature selection module that employs a correlation based feature selection algorithm (21). These feature vectors along with their corresponding labels are then forwarded to tune a classifier. In this study, a diverse group of classifiers such as probabilistic (Naive bayes), functional (Multilayer perceptron[MLP]), and decision tree (Random Forest), are utilized (see (22) for details).

Spot Detection with Learned Designs (P-2)

Based on expert intuition and experience, features extracted in P-1 can be subjective. Therefore, the key goal of P-2 approaches is to *automatically* learn the most optimal spot feature representation from the data. Neural networks are a well-known example of P-2 approaches.

Deep CNN (16,23) have been highly successful in many image-based ML studies. Unlike P-1, these features are hierarchically learned in multiple layers in an automatic fashion and not hand-crafted by experts. Consider, $M = f()$ as an overall classification model learned by a P-2 approach. In deep neural networks, f can be decomposed into multiple functional layers:

$$f() = (f_u \circ f_{(u-1)} \circ f_{(u-2)} \circ \ldots \circ f_1). \qquad [1]$$

Each function, f_j, $j \in [1, u]$, can represent a (a) convolutional layer, (b) nonlinear gating layer, (c) pooling layer, (d) full-connected layer (see (16,23,24) for more details). For a given task, weights for these convolutional filters are learned automatically using the training data.
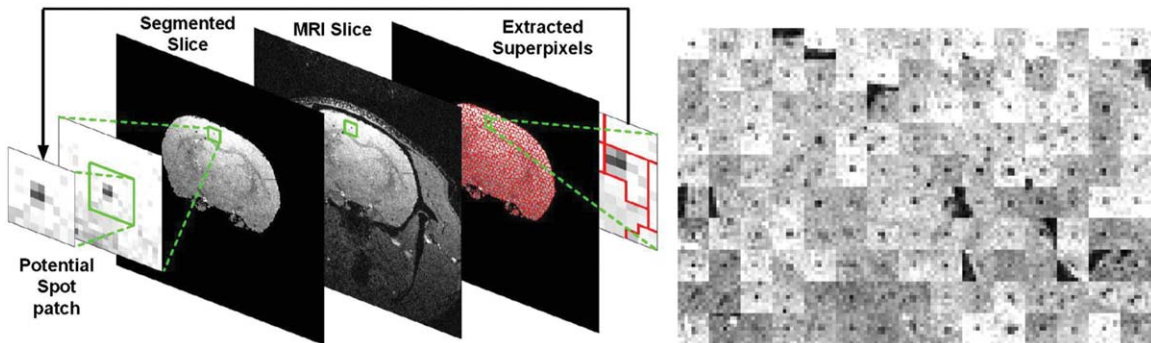

FIG. 3. (Left) Illustrating the generation of candidate regions. For each superpixel a candidate patch is extracted. The darkest pixel in the superpixel acts as the center of the patch. (Right) A mosaic of several 9 × 9 patches extracted from an MRI slice. It can be seen that all patches have a dark region in the center representing a spot in a 2D slice.

Table 2
Experimental Comparison of In Vivo Spot Detection Performance Using P-1 and P-2

	Algorithms	J_1	J_2	J_3	J_4	J_5	J_6	Means
P-1	Random Forest	94.0	86.9	95.3	94.1	86.0	94.7	91.8 ± 4.2
	Naive Bayes	82.9	81.8	84.3	84.1	80.1	83.7	82.8 ± 1.6
P-2	CNN	**96.4**	**92.3**	**96.1**	**96.4**	**91.2**	95.0	**94.6 ± 2.3**
	MLP	91.1	85.2	90.9	91.4	84.2	90.3	88.9 ± 3.3
	MLP (P-1/2)	93.9	89.4	95.8	95.4	90.0	**95.7**	93.4 ± 2.9
Means		91.7 ± 5.2	87.1 ± 4.0	92.5 ± 5.0	92.3 ± 4.9	86.3 ± 4.5	91.9 ± 5.0	

The best performance on each testing set is represented in bold.

Different architectures of a CNN are created by utilizing different number of layers and also by sequencing these layers differently. CNN architectures also vary depending on the choice of the nonlinear gating function. Filter sizes for convolutional layers are also determined depending on the application at hand. Well-known CNN architectures such as AlexNet (23) or GoogLeNet (25) cannot be utilized for spot detection in MRI. Therefore, a new CNN architecture, specifically designed for spot detection in MRI, is proposed here. The proposed CNN architecture has three composite layers and 1 fully connected layer (see Supporting Information Fig S5). Each composite layer consists of a convolutional layer and a gating function. Note that in a conventional CNN architecture, a pooling layer is also used which reduces the dimensionality of the input data. However, a pooling layer is not utilized in this architecture due to the small size of the input patches (9×9). Using a pooling layer, in this context, may result in the loss of valuable information which may be essential to be utilized by the next layers. Further, a gating function is usually added for introducing nonlinearity into a CNN. Without nonlinear gating, a CNN can be seen as a sequence of linear operations which can hinder its ability to learn the inherent nonlinearities in the training data. In conventional neural networks, a sigmoid function or a hyperbolic tangent function was generally utilized for this purpose. However, in recent studies, utilizing ReLU (Rectified Linear Units) has shown significantly superior results for this role (23). Therefore, the proposed architecture uses ReLU as a nonlinear gating function.

Further customizing to the task at hand, the sizes of all the convolutional filters were kept small. However, their numbers were kept high. The goal was to provide a higher capacity to the CNN architecture for capturing a diverse set of local features of a patch. Filter sizes and dimensions of resulting feature maps can be seen in Supporting Information Figure S5. For any task i, the proposed model (CNN architecture) can be written as

$$M = (\gamma \circ L_{\text{fc}} \circ \beta \circ C^{i3} \circ \beta \circ C^{i2} \circ \beta \circ C^{i1}). \qquad [2]$$

where γ represents a standard softmax function that can be applied to the output of the fully connected layer L_{fc}. β denotes the nonlinear gating function and C^{ik} represents the convolutional layer in the composite layer k.

Performance of the Two Paradigms

Experiments were performed to answer the following main questions: (1) Which of the two ML technique results in the best detection accuracy for in vivo spots in MRI? (2) How does the best approach perform on in vitro evaluation studies? (4) Can a ML approach learned on in vivo *data* be tested for spot detection on in vitro data? (5) How is the performance affected if the MRI is conducted at low resolution? (6) Is the proposed approach robust to the differences in MRI machines in terms of field strength, make and model etc.? Importantly, it is also of interest to investigate how the theoretically computed number of spots for in vitro MRI scans compares with the automatically detected spot numbers.

In Vivo Evaluation Studies

In this study, the spot classification performance of a diverse set of approaches was evaluated using the two sets of in vivo MRI scans, i.e., G_A and G_B. First, experiments and results are discussed for G_A that has five different MRI scans obtained from one MRI machine and labeled by one expert. Three of these in vivo scans contain spots that were manually labeled by experts whereas the remaining two were naive. Six combinations of testing and training *pairs* are created such that two scans are always present in the testing set of each pair, where one of the scans is a naive and the other contains spots. The remaining three out of the five scans are used for training the ML algorithms. Area Under the Curve (AUC) is utilized as a standard measure for classification accuracy. Experimental results for all the algorithms are listed in Table 2.

It was observed that the best results were achieved by a CNN, with a mean accuracy of 94.6%. The superior performance of CNN can be mainly attributed to its ability to automatically explore the most optimal features using training data rather than relying on hand-crafted features utilized in traditional machine learning. Second, CNN learn features in a deep hierarchy across multiple layers. Recent research shows that such a hierarchy provides a superior framework to CNN for learning more complex concepts, unlike traditional machine learning approaches which learns in a shallow manner ((23–25).

The second best results were observed with the simple MLP approach when it takes the carefully designed, handcrafted features as an input, rather than the raw data X. This MLP can be viewed as a mixed paradigm approach (P-1/2). However, the deep learning CNN that inherently extracts hierarchical features without using any hand-crafted features resulted in the overall best performance. CNN detected a total of 5246, 5719, and 16,048 spots in the three labeled rats of G_A.
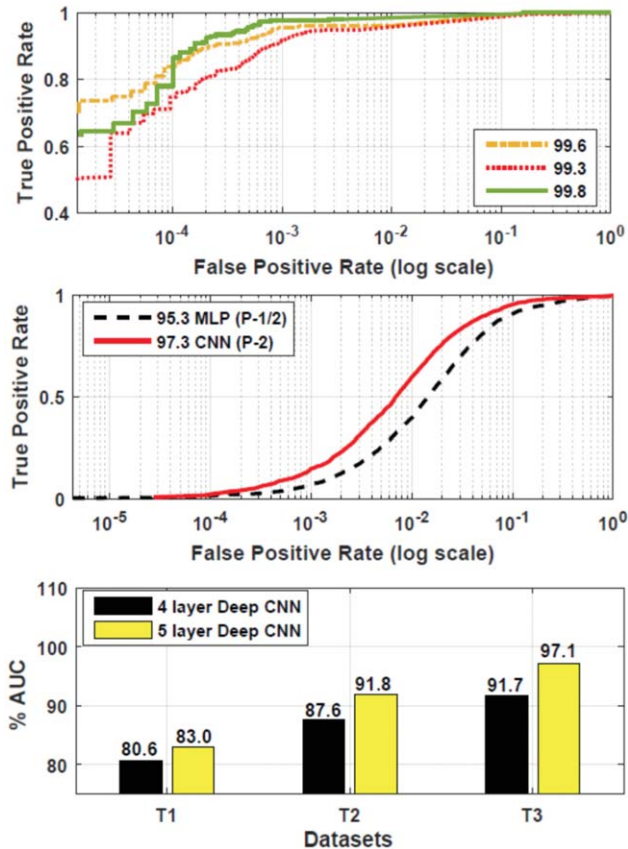
FIG. 4. (Top) Receiver operating characteristic (ROC) curve is shown for results obtained on 3 in vitro scans (100 micron resolution), with inset indicating individual percent accuracies (AUC) for each data set, (Middle) ROC curves for a generalization test using in vivo scans, with inset indicating individual percent accuracies (AUC) for each approach, (Bottom) Comparing accuracies on low resolution MRI scanning for in vitro data (200 micron resolution).

Probabilistic Naive bayes, using P-1, shows the worst detection performance with an average accuracy of 82.8%. This can be because naive bayes assumes complete independence between the features which in many practical problems may not be true. Further, it can be seen in Table 2 that J_2 and J_5 testing sets proved to be the most challenging with low mean accuracies of 87.1% and 86.3%, respectively, from all algorithms. Dataset J_4 resulted in the overall best performance with mean accuracy of 92.5%. When investigating this, it was found that both J_2 and J_5 contained MRI scan G_{A1} in their test set accompanied with a different naive scan. It was seen that the labeled patches in G_{A1} were significantly more challenging in terms of morphology and intensity than those extracted from other scans.

The best two approaches, i.e., MLP (P-1/2) and deep CNN (P-2), were then further compared using another set of in vivo scans i.e., G_B. This data was collected from a different machine having a different field strength and was also labeled by a different expert. In this study, all the previous five scans of G_A were used for training both approaches (creating a larger training set), and then the learned spot detection models were tested on the in vivo scans in $G_B = \{G_{B1}, G_{B2}\}$. Note that despite the differences in machine, its field strength, and also the labeling

expert, CNN performed best with an accuracy of 97.3% whereas the mixed paradigm MLP (P-1/2) achieved 95.3%. We show the ROC curves for this test in Figure 4. In G_B, the total number of spots detected by CNN was 4930.

In Vitro Evaluation Studies

It can be observed that CNN yields the best result on the in vivo datasets despite the simplicity of its approach. In this study, its performance is evaluated on the in vitro data in set G_C and G_D. Its performance is first tested on G_C that has four in vitro MRI scans each with a 100μm resolution creating a 3D matrix of $(128 \times 80 \times 80)$. Using these four scans, three different testing and training pairs were developed. Each testing and training pair has two MRI scans. The naive MRI scan was always kept in the test set, thereby generating three combinations with the remaining other sets. It was observed that CNN performed with a mean accuracy of 99.6% on in vitro scans. The individual ROC plots for these tests are shown in Figure 4.

A different study was then conducted to see the degradation in performance when each of the four in vitro scans are obtained with a much lower resolution of 200μm creating a matrix of $(64 \times 40 \times 40)$. Such a study is desirable as in some practical applications it may be more convenient to rapidly obtain an MRI at a lower resolution, particularly in human examinations. Using the same procedure as before, three different testing and training pairs were created. It was noted that the mean performance decreased to 86.6%±5.6. However, it was also seen that when the number of learning layers for CNN was increased to 5 (4 composite and 1 fully connected) the performance improves to 90.6%±7.1. The individual improvements on all the three sets are shown in Figure 4.

Comparison with Theoretically Computed Spot Numbers

A comparison between the automatically detected number of spots with the theoretically computed number of spots was conducted using 25 in vitro MRI scans of set G_E. This is an important experiment as it allows a *direct comparison* with the actual number of injected spots. All the available data from G_A to G_D was used for training a CNN and then the trained CNN model was used for testing on these 25 scans in set G_E. Each scan is expected to contain about 2400 spots. However, it is important to understand that due to the use of manual procedures, the actual number of spots may vary about 2400. The results of automatic spot detection are tabulated in Table 3 under different MRI conditions.

Model Generalization Studies

In this section, the generalization ability of the proposed approach is determined by testing it in different possible practical scenarios. In practice, in vivo scans might be collected with different MRI machines at different laboratories using different field strengths. G_A and G_B represent two such in vivo datasets. As discussed before in the in vivo evaluation studies, and as shown in Figure 4, the CNN based approach demonstrates robustness to

Table 3
Automatically Detected Number of Spots in Five Samples Under
Five Conditions

Condition	Tube 1	Tube 2	Tube 3	Tube 4	Tube 5
TE 10	2147	2272	2474	2152	2270
TE 20	2608	2750	3039	2644	2660
TE 30	2844	2993	3272	2809	2909
TE 10 (Low SNR)	1982	2023	2247	1949	2014
TE 20 (Low SNR)	2419	2563	2794	2401	2445

The theoretically expected number of spots in each sample is
2400.

such variations and achieves 97.3% accuracy despite such differences. Further, it is necessary to know how the performance would be affected if in vivo data is used for training but the in vitro data is used for testing. Therefore, an experiment was conducted where a CNN was trained using G_A (in vivo) and then tested it using G_C (in vitro). CNN still performed with an accuracy of 96.1%. An in vivo and in vitro MRI slice with automatically detected spots is shown in Figure 5.

Spot Detection with Transfer Learning (P-3)

The success of deep learning methods for a specific application depends on the availability of *large scale* annotated datasets. Unfortunately, in many applications, especially those related to medical imaging and radiology, obtaining a *large scale* annotated (e.g., labeled) dataset can be challenging. Therefore, the focus here is devising a strategy to improve the accuracy of a CNN trained only on limited samples.

The concept of transfer learning (24,26), or inductive transfer, entails the transfer of knowledge from a *source* task (e.g., document classification) to a *target* task (e.g., voice recognition). In this article, transfer learning is exploited in the context of stem cell detection in MRI data (i.e., spot detection), where there is scarcity of labeled training data. Here, transfer learning is implemented via CNNs and involves transplanting network layers from one CNN (derived from the source task) to another (spot detection—known as the target task). The proposed approach is explained below and the basic architecture of this approach is shown in Figure 6.

First, in addition to the target data, i.e., the given MRI data X, the data of unrelated 20 different real world *source* entities were collected from publicly available databases (27). These include images of entities such as soccer ball, cherry, egg, cat, bananas, and soforth. (see Supporting Information Fig. S6 for all names). The data of each source i is denoted as X_i where $i \in \{1, 2, \ldots, 20\}$.
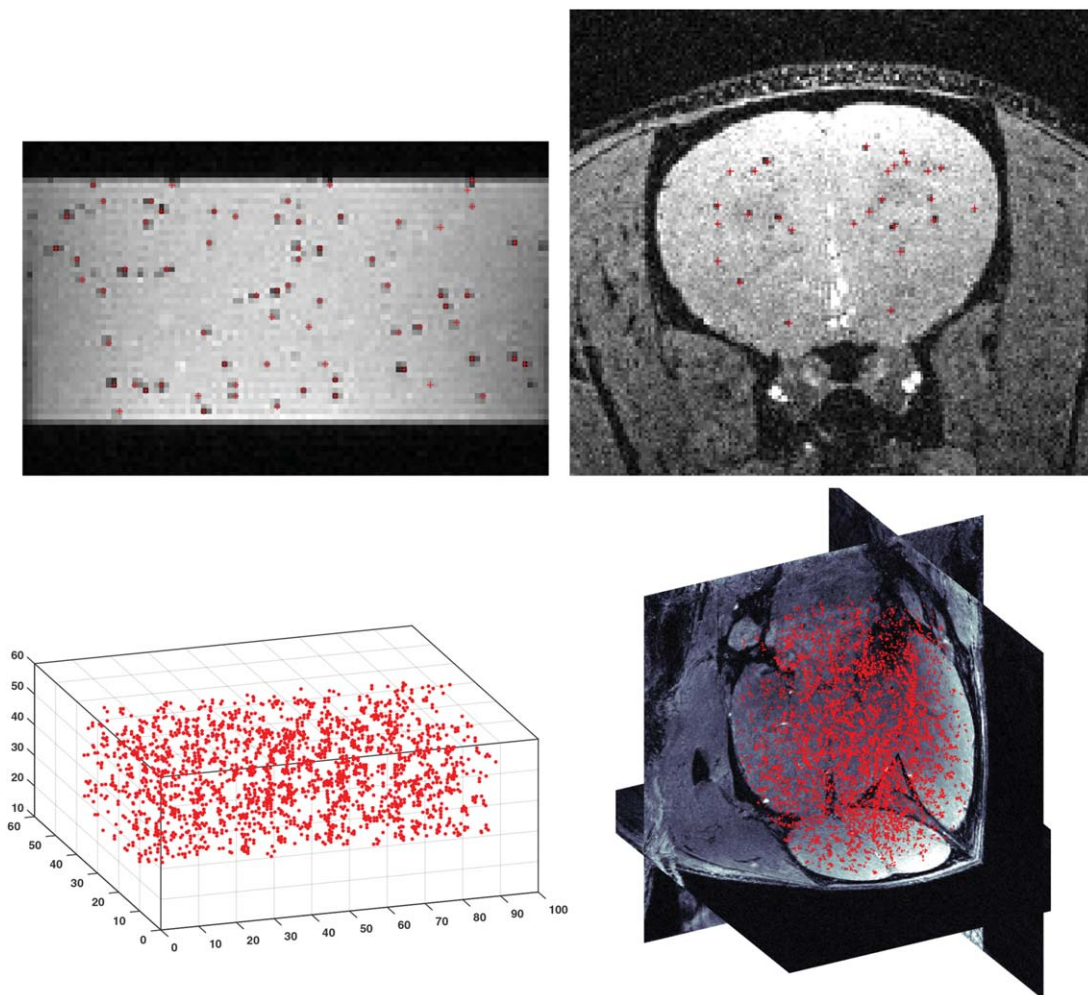

FIG. 5. Automatic spot detection and visualizations: (left) in vitro, (right) in vivo.
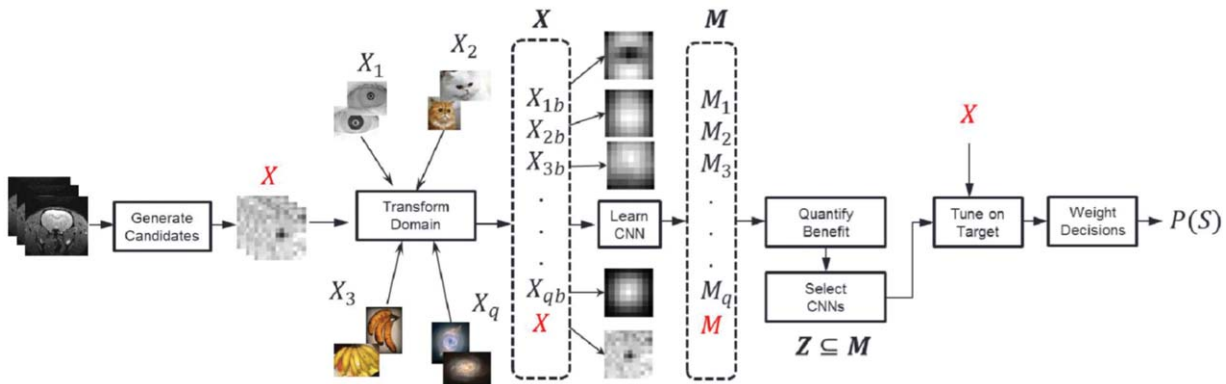
FIG. 6. Architecture of the transfer learning based approach.

Second, the data from these source tasks were geometrically transformed to ensure compatibility with the target task patches. Therefore, the images in X_i for each source i were transformed to 9×9 patches. This transformation is functionally denoted as $T(X_i)$. It was observed that many of the down-sampled images display a spot-like pattern (as shown in Supporting Information Fig. S7). However, these spots exhibit differences in their shape, size, and intensity and, therefore, present completely different distributions.

Third, for each X_i, a two-class dataset $X_{ib} = \{T(X_i), T(B_g)\}$ was developed. $T(X_i)$ consists of samples of one class (positive), while $T(B_g)$ consists of samples of the second class (negative). Images for the negative class, B_g, were selected using a popular search engine by querying the following entries: (a) texture and patterns, (b) sky and ocean, (c) grass. It was observed that the transformed images of these categories show visually rough or uniform characteristics similar to that of the nonspot patches. Collectively, all the obtained datasets can be denoted as $\mathbf{X} = [X, X_{1b}, X_{2b}, \ldots, X_{20b}]$.

Fourth, based on each two-class dataset X_{ib}, a binary classification task was defined. The goal of this task was to learn a CNN M_i that can distinguish between patches in $T(X_i)$ and $T(B_g)$. Generally, to learn a CNN, the weights in all of its layers are first randomly initialized. Let this be denoted as M_R. Given a dataset X_{ib}, these weights are iteratively changed. This learning can be functionally denoted as $M_i = \Theta(M_R, X_{ib})$.

Consequently, a set of 20 different source CNNs $\{\cup M_i\}_{i=1}^{20}$ can be learned. Using this approach, a CNN $M = \Theta(M_R, X)$ can also be learned to differentiate between spot and nonspot patches. Collectively, the set of learned CNNs can be denoted as $\mathbf{M} = [M, M_1, M_2, \ldots, M_{20}]$. Conversely, CNNs can also be learned without using a randomly initialized network. For example, a CNN M_{xi} that can distinguish between spot and nonspot patches can also be learned, i.e., $M_{xi} = \Theta(M_i, X)$. This means, that the weights already learned for a source task i are *transferred* to initialize another CNN whose goal is to learn to distinguish between spot and nonspot patches (target task). This transfer provides a more useful starting point in learning a target CNN and, thus, results in better generalization of the learned CNN. However, previous research shows that transferring from

some source tasks may be significantly more beneficial than that from others (24).

Therefore, as a fifth step, the proposed approach automatically determines which source CNN would be the *most beneficial* for transfer. There is no previous literature that shows how to automatically rank the available source CNNs based on their predicted benefit to the target task. Note that this is not a learning problem where an objective function can be stated and then optimized using the training data. Instead, it requires a *zero-shot* prediction which is a challenging task. The approach adopted here automatically measures the potential usefulness of each source CNN, M_i, by measuring its characteristic E_i prior to conducting transfer, where:

$$E_i = \{\lambda J_i + (1 - \lambda)U_i\}. \qquad [3]$$

J_i measures how *different* is the learned information (CNN weights) of a source CNN M_i from the target CNN M whereas U_i measures how discriminating is a source CNN M_i for the target task. For details on computing J_i and U_i, see the Supporting Information on *source CNN selection*.

To the best of our knowledge, this is the first attempt at ranking source CNNs for a given target task. Note that λ is simply a weighting parameter. In this study, $\lambda = 0.8$ was used in all the experiments. Finding an optimal value of λ is not the focus here; however, a more optimal value may result in even better performance.

As a final step, either the top CNN M_i or a *group* of the top $q \in \{2, \ldots, 20\}$ sources can be selected for transfer. The selected top q sources makes a group $Z \subset M$. When using a *group*, the predictions of the multiple models are fused using a standard probabilistic approach by utilizing the corresponding E_i for each source CNN M_i as a prior in a Bayesian formulation.

Performance of P-3

In this section, experiments were conducted to answer the following questions: (1) Does the spot detection benefit from transfer learning when the annotated training data is very limited? (2) Is the ranking of source CNNs prior to transfer, a beneficial procedure? (3) Why is it
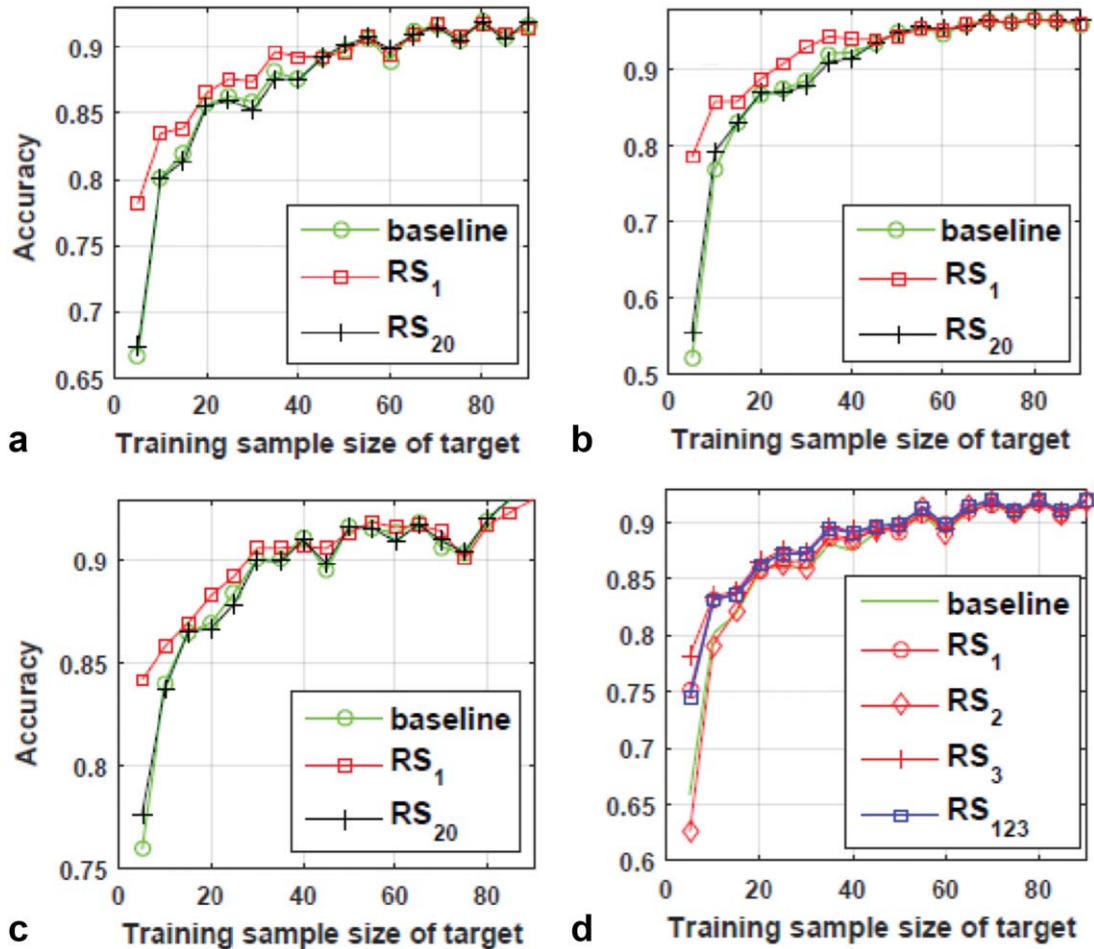
FIG. 7. Source ranking for transfer learning. **a–c**: Demonstrate the benefit of ranking source CNNs before transfer when the training data is sparse. **d**: Represents the case where information fusion provides robustness to ranking mistakes.

useful to combine information from CNNs learned from different sources?

In Figure 7a–c, using all of the three labeled datasets of G_A, three different testing scenarios are shown. On the x-axis, the amount of training data was varied and on the y-axis the performance of differently trained CNNs was observed. The baseline method is a CNN that did not undergo any transfer learning and only used the target data for training. The remaining two CNNs underwent transfer learning with the best ranked (RS_1) and worst ranked (RS_{20}) sources, respectively. We observed that the performance gain due to transfer from the best source is significantly higher when the training data from the target dataset is small. For example, in Figure 7b, using only 5% of the training data, the accuracy substantially improved from 52% to nearly 78% on the test set. Such an increase is highly encouraging in the clinical arena where there is scarcity of data and, where, the proposed approach would be highly relevant.

Next, we noted that the source which was ranked the "best" significantly outperforms the source which was ranked the "worst." Thus, our strategy to rank each source prior to invoking the transfer learning paradigm is clearly of importance. Further, we observed that choosing a *group* of top ranked CNNs can be more useful than simply

choosing one. In one scenario, the proposed approach mistakenly ranked one source as the second best as shown in Figure 7d. However, it can be seen that the decision weighting of multiple sources resulted in a performance that was significantly better than the worst source when there is limited target training data. In fact, at many points along the x-axis, we find that the resulting performance was higher than the other two sources as well.

DISCUSSION

Automated spot detection presents a set of unique challenges that were carefully considered while designing computer vision and machine learning-based approaches.

First, for thorough evaluation and training, an annotated MRI database needed to be developed. Therefore, a diverse database consisting of 40 MRI scans was assembled and more than 19,700 manual labels were assigned.

Second, given an MRI scan, a set of candidate regions needed to be extracted effectively. Each candidate region must represent a region in MRI that can potentially contain a spot. This article discussed how a superpixel based strategy can be designed to extract relevant regions. The proposed approach has clear advantages over some traditional alternatives.

Third, spots have high intra-class variation due to their diverse appearances in terms of shape and intensity. Therefore, for machine learning approaches to work effectively, a set of robust feature descriptors needed to be extracted from the candidate regions. A novel CNN architecture was designed to automatically extract the most useful spot features. The performance of these features was systematically compared against those extracted by appropriating hand-crafted feature extraction techniques. Results show that automatically learned features performed better with an accuracy of up to 97.3% in vivo.

Fourth, machine learning approaches typically require a large training dataset for accurate learning. However, in applications in the medical domain, it can be challenging to obtain a large volume of training data. Therefore, this article explored how automatic spot detection can be performed using a limited amount of training data. A novel transfer learning strategy for CNNs was developed, where the best source task is automatically selected from an ensemble of many tasks.

It is important to note that MRI-based cell tracking has remained largely phenomenological for its history, starting in the late 80s. Moving forward, automated spot detection for MRI-based cell tracking would prove useful across a broad spectrum of research tracks. For example, Walczak et al., infused neural stem cells via the carotid artery in an effort to target stroke lesions (28). High resolution in vivo and in vitro MRI appear to show small clusters of cells, perhaps even single cells, distributed in the brain as a function of the intervention. Only qualitative analysis was performed on this imaging data; automated spot detection would have enabled quantitative metrics of cell numbers. Another application would be for the evaluation of transplanted islets encapsulated with iron oxide nanoparticles within alginate microspheres. These imaging features, typically are individual hypointensities, examples being (29) and (30). In both cases, only qualitative or semiquantitative data were compiled, without a direct enumeration of transplanted and surviving grafts. A last example would be for enumeration of kidney glomeruli in conjunction with the use of cationized ferritin as a contrast agent (31).

The general use of MRI-based cell tracking and this specific approach to quantifying this data has some limitations. Still, MRI of magnetically labeled cells only detects the iron, not the cell itself, and this method is still unable to distinguish live cells from dead cells. Further, if more than one cell generates a particular spot in the MRI, then the calculated cell number would be inaccurate. In this work, only 67% of spots were resultant from individual cells, the other 33% from two or three cells. It remains an open question as to how accurate an automated spot detection algorithm for MRI-based cell tracking needs to be to provide useful clinical information. However, we do not feel that heterogeneous magnetic cell labeling is a significant problem. Indeed, cells with more internalized iron would have darker and larger spots on MRI, while cells with less internalized iron would have lighter and smaller spots. However, our automated quantification algorithm can account for differences in spot size and intensity to compensate for heterogeneous cell labeling.

CONCLUSION

In summary, this article presented a comprehensive study on spot detection in MRI using ML approaches. Challenges unique to spot detection in MRI were highlighted. Novel approaches were designed for spot detection using different ML paradigms and were then experimentally compared. For this study, a new labeled database of MRI scans was developed. Results show that features that are automatically learned using a deep-learning approach outperform hand-crafted features. It was also observed that the transfer learning paradigm can provide significant performance improvement when the training dataset is small. Further, using deep CNNs, the proposed approach achieved up to 97.3% accuracy in vivo and about 99.8% in vitro.

REFERENCES

1. Clinical trial: Outcomes Data of Adipose Stem Cells to Treat Parkinson's Disease. https://clinicaltrials.gov/ct2/show/NCT02184546 (First received: July 3, 2014 Last updated: June 17, 2015 Last verified: June 2015).
2. Clinical trial: A Study to Evaluate the Safety of Neural Stem Cells in Patients with Parkinson's Disease. https://clinicaltrials.gov/ct2/show/NCT02452723 (First received: May 18, 2015 Last updated: March 10, 2016 Last verified: February 2016).
3. Clinical trial: Umbilical Cord Tissue-derived Mesenchymal Stem Cells for Rheumatoid Arthritis. https://clinicaltrials.gov/ct2/show/NCT01985464 (First received: October 31, 2013 Last updated: February 4, 2016 Last verified: February 2016).
4. Clinical trial: Cx611-0101, eASCs Intravenous Administration to Refractory Rheumatoid Arthritis Patients. https://clinicaltrials.gov/ct2/show/NCT01663116 (First received: August 5, 2011 Last updated: March 5, 2013 Last verified: February 2013).
5. Clinical trial: Evaluation of Autologous Mesenchymal Stem Cell Transplantation (Effects and Side Effects) in Multiple Sclerosis. https://clinicaltrials.gov/ct2/show/NCT01377870 (First received: June 19, 2011 Last updated: April 24, 2014 Last verified: August 2010).
6. Clinical trial: Stem Cell Therapy for Patients with Multiple Sclerosis Failing Alternate Approved Therapy- A Randomized Study. https://clinicaltrials.gov/ct2/show/NCT00273364 (First received: January 5, 2006 Last updated: March 21, 2016 Last verified: March 2016).
7. Clinical trial: Pilot Study of Redirected Autologous T Cells Engineered to Contain Humanized Anti-CD19 in Patients with Relapsed or Refractory CD19+ Leukemia and Lymphoma Previously Treated with Cell Therapy. https://clinicaltrials.gov/ct2/show/NCT02374333 (First received: February 23, 2015 Last updated: February 23, 2016 Last verified: February 2016).
8. Clinical trial: Genetically Modified T-cells in Treating Patients with Recurrent or Refractory Malignant Glioma. https://clinicaltrials.gov/ct2/show/NCT02208362. Last accessed December 2016.
9. Slotkin JR, Cahill KS, Tharin SA, Shapiro EM. Cellular magnetic resonance imaging: nanometer and micrometer size particles for noninvasive cell localization. Neurotherapeutics 2007;4:428–433.
10. Shapiro EM, Sharer K, Skrtic S, Koretsky AP. In vivo detection of single cells by MRI. Magn Reson Med 2006;55:242–249.
11. Zhou R, Djaudat I, Steen M, Curt C, Hualei Z, Hui Q, Jia Z, Michael G. SWIFT detection of SPIO labeled stem cells grafted in the myocardium. Magn Reson Med 2007;63:1154–1161.
12. Wu YL, Ye Q, Eytan DF, Liu L, Rosario BL, Hitchens TK, Yeh FC, Ho C. Magnetic resonance imaging investigation of macrophages in acute cardiac allograft rejection after heart transplantation. Circ Cardiovasc Imaging 2013;6:965–973.

13. Mori Y, Chen T, Fujisawa T, Kobashi S, Ohno K, Yoshida S, Tago Y, Komai Y, Hata Y, Yoshioka Y. From cartoon to real time MRI: in vivo monitoring of phagocyte migration in mouse brain. Sci Rep 2014;4:6997.

14. Smal I, Loog M, Niessen W, Meijering E. Quantitative comparison of spot detection methods in fluorescence microscopy. IEEE Trans Med Imaging 2010;29:282–301.

15. Afridi MJ, Liu X, Shapiro EM, Ross A. Automatic in vivo cell detection in MRI. In Proceedings of 18th International Conference on Medical Image Computing and Computer Assisted Intervention (MICCAI), Munich, Germany, 2015;391–399.

16. Taigman Y, Ming Y, Marc'Aurelio R, Lars W. Deepface: closing the gap to human-level performance in face verification. In Proceedings of the IEEE Conference on Computer Vision and Pattern Recognition (CVPR), Columbus, Ohio, USA, 2014. pp. 1701–1708.

17. Afridi MJ, Liu X, McGrath JM. An automated system for plant-level disease rating in real fields. In Proceedings of 22nd International Conference on Pattern Recognition (ICPR), Stockholm, Sweden, 2014. pp. 148–153.

18. Sorokin A, Forsyth D. Utility data annotation with amazon mechanical turk. In Proceedings of the IEEE Conference on Computer Vision and Pattern Recognition (CVPR), Anchorage, Alaska, USA, 2008. pp. 1701–1708.

19. Shapiro EM, Skrtic S, Koretsky AP. Sizing it up: cellular MRI using micronsized iron oxide particles. Magn Reson Med 2005;53:329–338.

20. Witten IH, Frank E. Data mining: practical machine learning tools and techniques. In: Morgan Kaufmann, Burlington, Massachusetts, USA. 2005. pp. 3–607.

21 Hall MA. Correlation-based feature selection for machine learning, Doctoral dissertation, The University of Waikato, 1999.

22. Bouckaert R, Frank E, Hall M, Kirkby R, Reutemann P, Seewald A, Scuse D. Weka manual for version 3-7-8, 2013.

23. Krizhevsky A, Ilya S, Geoffrey EH. Imagenet classification with deep convolutional neural networks. In Proceedings of the Neural Information Processing Systems Conference, Lake Tahoe, Nevada, USA, 2012. pp. 1097–1105.

24. Yosinski J, Jeff C, Yoshua B, Hod L. How transferable are features in deep neural networks? In Proceedings of the Neural Information Processing Systems Conference, Montreal, Canada, 2014. pp. 3320–3328.

25. Szegedy C, Liu W, Jia Y, Sermanet P, Reed S, Anguelov D, Erhan D, Vanhoucke V, Rabinovich A. Going deeper with convolutions. In Proceedings of the IEEE Conference on Computer Vision and Pattern Recognition (CVPR), Boston, Massachusetts, USA, 2015, pp. 1–9.

26. Pan SJ, Qiang Y. A survey on transfer learning. IEEE Trans Knowl Data Eng 2010;22:1345–1359.

27. Deng J, Dong W, Socher R, Li LJ, Li K, Fei-Fei L. Imagenet: a large-scale hierarchical image database. In Proceedings of the IEEE Conference on Computer Vision and Pattern Recognition (CVPR), Miami, Florida, USA, 2009. pp. 248–255.

28. Walczak P, Zhang J, Gilad AA, Kedziorek DA, Ruiz-Cabello J, Young RG, Pittenger MF, van Zijl PC, Huang J, Bulte JW. Dual-modality monitoring of targeted intraarterial delivery of mesenchymal stem cells after transient ischemia. Stroke 2008;39:1569–1574.

29. Arifin DR, Valdeig S, Anders RA, Bulte JW, Weiss CR. Magnetoencapsulated human islets xenotransplanted into swine: a comparison of different transplantation sites. Xenotransplantation 2016;23:211–221.

30. Wang P, Schuetz C, Vallabhajosyula P, et al. Monitoring of allogeneic islet grafts in nonhuman primates using MRI. Transplantation 2015; 99:1574–1581.

31. Baldelomar EJ, Charlton JR, Beeman SC, Hann BD, Cullen-McEwen L, Pearl VM, Bertram JF, Wu T, Zhang M, Bennett KM. Phenotyping by magnetic resonance imaging nondestructively measures glomerular number and volume distribution in mice with and without nephron reduction. Kidney Int 2016;89:498–505.

32. Liu MY, Tuzel O, Ramalingam S, Chellappa R. Entropy rate superpixel segmentation. In Proceedings of the IEEE Conference on Computer Vision and Pattern Recognition (CVPR), Colorado Springs, Colorado, USA, 2011. pp. 2097–2104.

33. Turk M, Pentland AP. Face recognition using eigenfaces. In Proceedings of the IEEE Conference on Computer Vision and Pattern Recognition (CVPR), Hawaii, USA, 1991. pp. 586–591.

34. Dalal N, Triggs B. Histograms of oriented gradients for human detection. In Proceedings of the IEEE Conference on Computer Vision and Pattern Recognition (CVPR), San Diego, California, USA, Vol. 1, 2005. pp. 886–893.

35. Oliva A, Torralba A. Building the gist of a scene: the role of global image features in recognition. Prog Brain Res 2006;155:23–36.

36. Bennewitz MF, Tang KS, Markakis EA, Shapiro EM. Specific chemotaxis of magnetically labeled mesenchymal stem cells: implications for MRI of glioma. Mol Imaging Biol 2012;14:676–687.

SUPPORTING INFORMATION

Additional Supporting Information may be found in the online version of this article.

Fig. S1. a, b: Single cells within plane c) cell through plane (**d, e**) two cells (**f**) 3 connected cells (**g, h, i**) showing cells bounded within blood vessels, with some at bifurcations; scale bars are 25 ums. Cropped from images with width of 300 um (no MPIO labeled MSCs were cropped from view).

Fig. S2. Similar to the concept of eigen faces (33), Principle Component Analysis (PCA) was utilized to extract eigen spot shapes using all of the 9 $\times$ 9 spot patches in the training set. The top PCA component for the spot patches obtained on three labeled rats in G_A are shown here. An iteratively increasing threshold is then applied on the values of these top PCA components to extract different binary patches that are utilized as filters to capture the shape and intensity information on spot patches.

Fig. S3. Binary shape filters are obtained using the top PCA components (shown in Fig. S2.). By iteratively increasing the threshold values from dark to light intensities, PCA components can result in different binary shapes. Domain experts agree that these binary filter patches represent many frequent shapes of the actual spots. All these patches are rotated and translated to obtain a large set of different shape filters. These filters are convolved with each candidate patch and the computed response is taken as a feature. A large set of these responses comprehensively captures the shape and intensity information of spot patches.

Fig. S4. Visual representation of context features for two context patches: While learning the definition of a spot, it may also be useful for a classifier to learn more about its surrounding context. Therefore, to capture the appearance of the patch's context, a larger patch of 21 $\times$ 21 was extracted around the center of a candidate patch x_i. Two well-known appearance descriptors in computer vision were then used to extract features: (a) Histogram of Gradients (HoG) and (b) Gist (34,35). A visual representation of HoG for two context patches is shown here. Red lines here indicate the different directions of intensity gradients whereas the lengths of the lines determine their magnitude.

Fig. S5. CNN architecture used in this work. The network takes a 9x9 image patch as input for a classification task i. Each composite layer L^k, $k \in \{1, 2, 3\}$, is composed of a convolutional layer C^{ik} which produces the feature maps F^{ik} and a non-linear gating function β producing the transformed feature maps F_β^{ik}. After passing through the composite layers, the net passes through the fully connected layer L^{fc} which produces the output. The *softmax* function is then applied to the output. Note that in the context of this work, this architecture represent the model M. The weights of all the filters across its processing layers are learned using the training data.

Fig. S6. Some convolution filters learned by the 2nd composite layers of our deep learning approach. Usually, each filter acts as a neuron and due to co-adaptation between a large number of such neurons, highly sophisticated features are extracted that can potentially model spot shape, intensity, texture etc.

Fig. S7. Transformed, average images for different source datasets.